electronics

MDPI

Article

Additive Manufacturing of a Miniaturized X-Band Single-Ridge Waveguide Magic-T for Monopulse Radar Applications

Riccardo Rossi [1], Roberto Vincenti Gatti [1,*], Flaviana Calignano [2], Luca Iuliano [2] and Simona Chiarandini [3]

[1] Department of Engineering, University of Perugia, Via G. Duranti 93, 06125 Perugia, Italy
[2] Department of Management and Production Engineering (DIGEP), Integrated Additive Manufacturing Center (IAM), Politecnico di Torino, Corso Duca Degli Abruzzi 24, 10129 Torino, Italy
[3] Elettronica Aster S.p.A., Via Longoni 110, 20825 Barlassina, Italy
* Correspondence: roberto.vincentigatti@unipg.it

Abstract: A low-profile single-ridge waveguide magic-T is proposed as a combination of two T-junctions at an X band. A slot coupling technique is used to reduce the component dimensions in the E-plane, thus leading to a low profile. The device can assume two configurations by arranging the sum and difference ports in the same or opposite direction, an attractive feature in the design of beamforming networks with complex routing. A magic-T prototype is fabricated using laser powder bed fusion additive manufacturing techniques. Good agreement between simulations and measurements is found.

Keywords: single-ridge waveguide; magic-T; low profile; X-band; additive manufacturing

Citation: Rossi, R.; Vincenti Gatti, R.; Calignano, F.; Iuliano, L.; Chiarandini, S. Additive Manufacturing of a Miniaturized X-Band Single-Ridge Waveguide Magic-T for Monopulse Radar Applications. *Electronics* **2023**, *12*, 1124. https://doi.org/10.3390/electronics12051124

Academic Editor: J.-C. Chiao

Received: 9 January 2023
Revised: 17 February 2023
Accepted: 22 February 2023
Published: 25 February 2023

1. Introduction

The waveguide magic-T is a four-port power dividing/combining device widely used in a variety of microwave systems due to a number of features such as input port matching, high output port isolation, amplitude and phase balance, low insertion loss, and high power-handling capacity [1]. This device can be obtained by combining an E-plane and an H-plane T-junction with common output co-linear ports. Since the four arms lie on two different planes, the overall component may be bulky, and the fabrication and assembly can be difficult. For this reason, the design of a compact magic-T is of great interest in all applications with stringent size requirements [2,3].

It is well known that, for a specified cutoff frequency, the introduction of a longitudinal conducting ridge along a waveguide reduces its width [4]. Nevertheless, to the authors' best knowledge, there is scarce literature about magic-T designs in ridge waveguide technology. The device [5] makes use of standard rectangular waveguide ports for all arms and, except for the sum port, stepped impedance transformers are required for matching, considerably increasing the overall dimensions. The waveguide height at the junction is halved for the co-linear inputs and the sum port is coupled by means of a ridge probe. Since this ridge waveguide section is relatively short and only used locally at the arms intersection, this component cannot be considered as a ridge waveguide implementation. A similar hybrid approach is proposed in [6], where a single-ridge waveguide section represents the difference port. Half-height rectangular waveguides are used for the co-linear arms, which are also bent to improve compactness. A standard rectangular waveguide is adopted for the sum port. In [7], single-ridge waveguide transmission lines are used for the co-linear and sum ports and a double-ridge section represents the difference port. A ridge tapering in the H-plane T-junction is responsible for the device matching. Double-ridge waveguides are used for all ports in [8], where matching is obtained by a proper ridge connection and a stepped transformer. Since conductive rods and capacitive strips are also needed at the junction for matching purposes, the fabrication can be quite challenging. Another full double-ridge waveguide implementation is reported in [9], which makes use

of two cylindrical posts at the arms intersection as matching elements. Stepped impedance transformers are needed at the sum and co-linear ports, thus increasing the device volume. A magic-T concept for additive manufacturing is presented in [10], using a pyramidal-ridge waveguide transmission line consisting of a trapezoidal waveguide cross section with a semicircular ridge. This is also a hybrid approach, as a rectangular waveguide section is adopted for the difference port.

In this paper, an X-band compact magic-T in single-ridge waveguide technology is presented for the first time. This component derives from a combination of two low-profile T-junctions in the E-plane and H-plane, also illustrated as a preliminary design step. The device develops on two layers which are coupled by means of a thin slot, thus making the structure quasi-planar. Similarly to [11,12], two architectures are proposed, which are referred to as T-shaped and cross-shaped (or X-shaped) according to the sum and difference ports pointing in the same direction or in opposite directions, respectively. This is an appealing feature in the design of any radar system where a low-profile monopulse comparator network is required [13–16]. The design choices of ridge waveguide technology and slot coupling lead to a very small-sized device, suitable for high-performance applications where compactness is also required. In addition to this, as matching elements are integrated in the waveguide layers, manufacturing is simplified with respect to referenced works. An X-shaped magic-T proof-of-concept prototype is fabricated using laser powder bed fusion (L-PBF) additive manufacturing technique of the aluminum alloy AlSi10Mg. Measured results are in good agreement with simulations, thus confirming the design procedure. All simulations are performed with the commercial full-wave software CST Microwave Studio.

2. T-Junctions

Since a magic-T can be seen as the superposition of an E-plane T-junction and an H-plane T-junction with common output ports, the design of these two devices is initially illustrated. In this paper, all components operate at the X band, and the selected center frequency is equal to 9.25 GHz with an operating bandwidth of 500 MHz. The ridge waveguide cross section is 13 mm $\times$ 5.5 mm, with ridge height and width both set to 4 mm. The ridge height remains unchanged along the waveguide branches for all devices. This waveguide choice allows for a very small size and leads to a cutoff frequency of 6.33 GHz, quite far from the design center frequency, thus also minimizing the insertion loss. The next higher-order mode cutoff frequency is equal to 21.21 GHz, thus providing a monomode bandwidth of 14.88 GHz. The proposed H-plane T-junction is depicted in Figure 1. Index one is the input port, while indices two and three stand for the output ports. The vacuum solid inside a metallic background is shown for better clarity. Similarly to quarter-wave impedance matching in microstrip T-junctions, the ridge widths are locally reduced to increase the impedance at the central section. Table 1 provides the H-plane T-junction geometrical parameters, while the simulated S-parameters are given in Figure 2.

The proposed H-plane T-junction shows a return loss better than 15 dB from 7.39 to 11.47 GHz. Due to the symmetry of the structure, equal power division is guaranteed over the entire simulated frequency range.

The proposed E-plane T-junction is depicted in Figure 3. Index one is the input port, while indices two and three stand for the output ports.

Table 1. H-plane T-junction geometrical parameters.

Parameter	Description	Value (mm)	Parameter	Description	Value (mm)
a	Waveguide width	13.00	rh	Ridge height	4.00
b	Waveguide height	5.50	rw	Ridge width	4.00
lm_1	Matching length 1	5.82	wm_1	Matching width 1	2.56
lm_2	Matching length 2	8.98	wm_2	Matching width 2	1.16

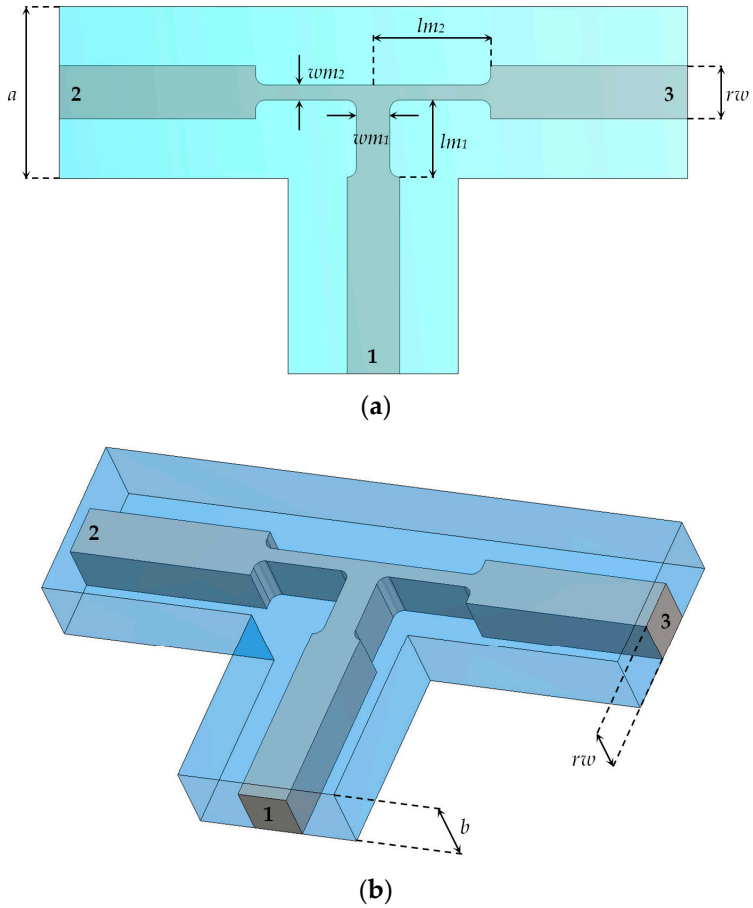

Figure 1. H-plane T-junction. (**a**) Top view. (**b**) 3D view.

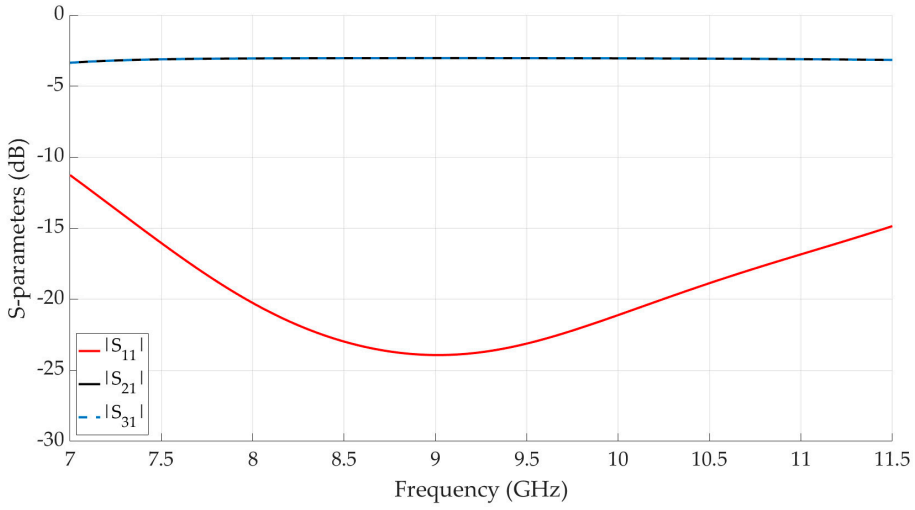

Figure 2. H-plane T-junction simulated S-parameters.

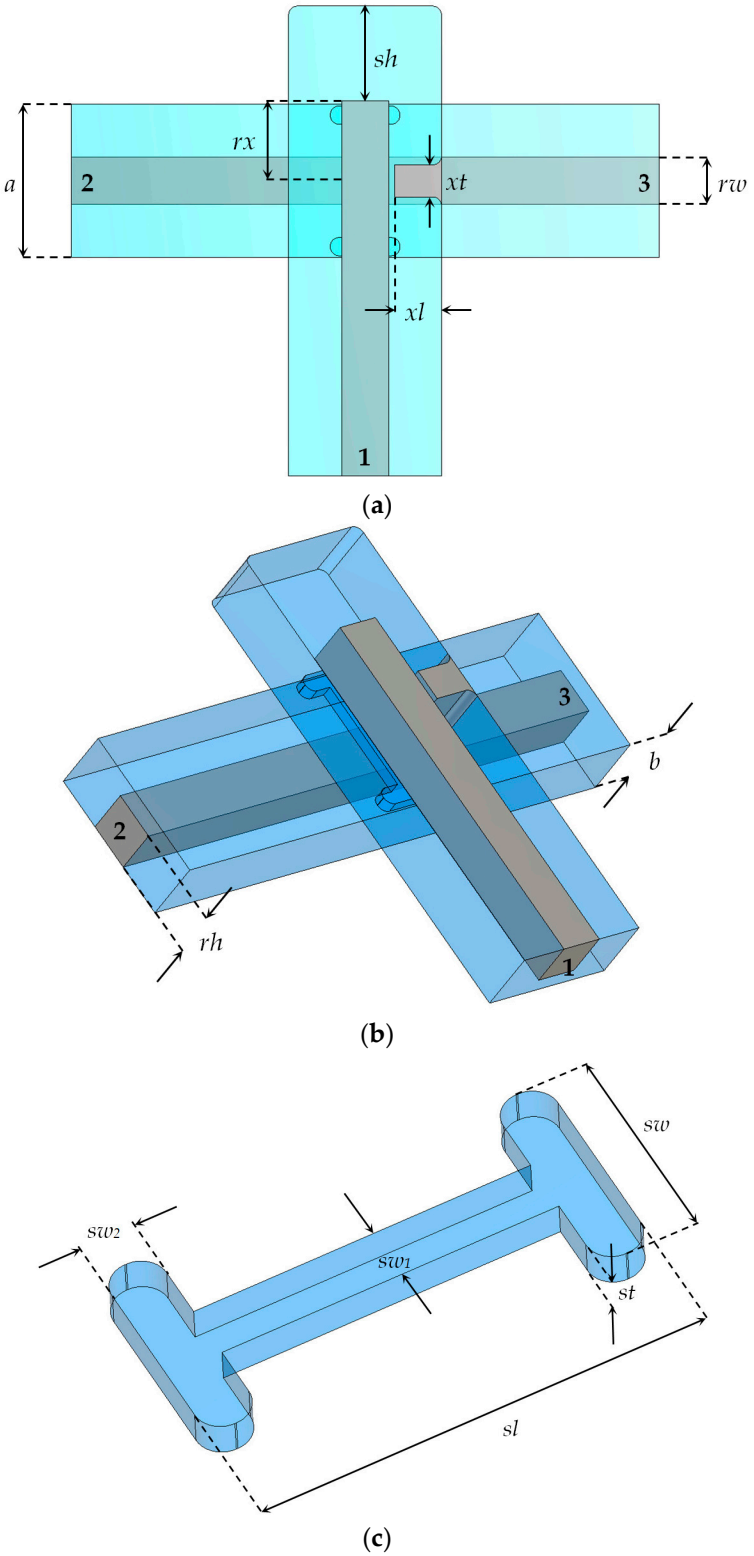

Figure 3. E-plane T-junction. (**a**) Bottom view. (**b**) 3D view. (**c**) 3D view (coupling slot).

The two waveguides are coupled through a symmetrical resonant H-shaped slot aligned with the upper waveguide centerline. The slot length *sl* affects the slot resonant frequency, and its value is space constrained by the lower waveguide broad wall, while the slot width *sw* contributes to the optimization of the input return loss. In addition to this, such a slot can be interpreted as a short double-ridge waveguide section with cutoff frequency of 7.74 GHz, thus allowing the field propagation between the two waveguide

layers. The slot is excited by a septum aligned with the lower waveguide centerline, presenting the same height as the waveguide. A stub is inserted by terminating the upper ridge on an open circuit at a proper distance from the waveguide short, thus simplifying the manufacturing process. Table 2 provides the E-plane T-junction geometrical parameters, while simulated S-parameters are given in Figure 4.

Table 2. E-plane T-junction geometrical parameters.

Parameter	Description	Value (mm)	Parameter	Description	Value (mm)
a	Waveguide width	13.00	*st*	Slot thickness	1.00
b	Waveguide height	5.50	*sw*	Slot width	5.92
rh	Ridge height	4.00	sw_1	Slot width 1	1.52
rw	Ridge width	4.00	sw_2	Slot width 2	1.54
rx	Ridge length	6.77	*xl*	Septum length	3.98
sh	Short distance	8.03	*xt*	Septum thickness	2.72
sl	Slot length	12.68			

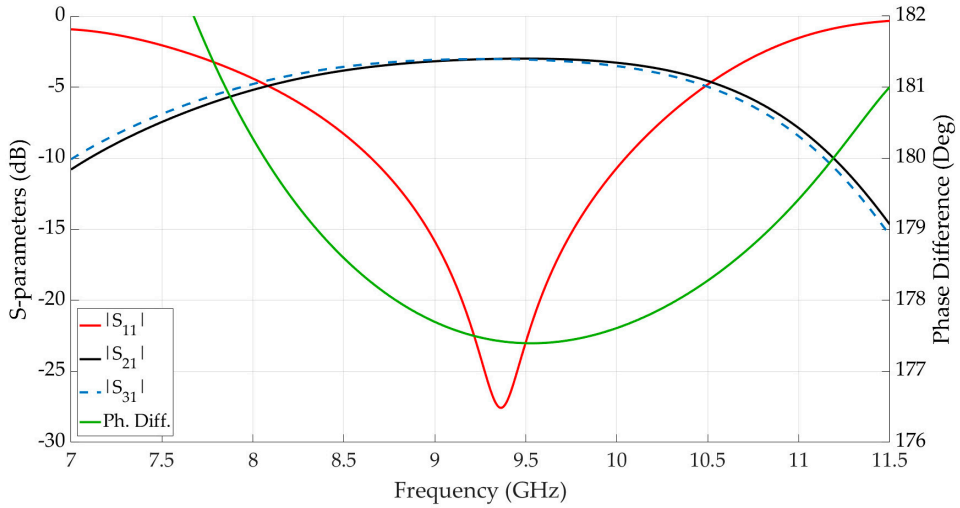

Figure 4. E-plane T-junction simulated S-parameters.

The proposed E-plane T-junction shows a return loss better than 15 dB from 8.96 to 9.76 GHz. A bandwidth reduction can be noticed with respect to the H-plane T-junction, and this is caused by the slot and the stub, which are resonant elements. Even though the septum introduces an asymmetry, the amplitude imbalance and the phase error between the two transmission coefficients are around 0.16 dB and 2.5 degrees in the same frequency range, respectively.

3. Magic-T

The E-plane T-junction and the H-plane T-junction of Section 2 can be combined to generate two magic-T architectures, namely the T-shaped (TSMT) of Figure 5a and the cross-shaped (X-shaped or XSMT) of Figure 5b, with sum and difference ports placed on the same or opposite sides, respectively. Port indices one, two, three, and four stand for the sum port, the co-linear ports, and the difference port.

With the same geometrical parameters listed in Tables 1 and 2, simulated scattering parameters for the resulting magic-T are good in terms of port matching and isolation. Nevertheless, a full-wave local optimization was performed for further improvement. Optimized geometrical parameters for the two magic-T architectures are listed in Table 3. In order to facilitate a fabrication process in the case of computer numerical control (CNC) milling machine manufacturing, internal edges were rounded by 0.75 mm while slot edges were rounded by 0.50 mm. The TSMT and XSMT volumes were 0.64 × 0.76 × 0.29 guided

wavelengths and 0.71 × 0.75 × 0.29 guided wavelengths, respectively. Contrary to the referenced works, where the difference port was orthogonal to the H-plane T-junction, both the presented devices were low-profile quasi-planar structures extending only 13 mm in height.

Simulated scattering parameters for the TSMT and XSMT are reported in Figures 6 and 7. In the frequency range 9–9.5 GHz, for both devices, the input matching is greater than 20 dB at all ports, the isolation between the co-linear ports is better than 20 dB, while the isolation between sum and difference port is better than 38 dB. As expected, a balanced power division with very low amplitude imbalances and phase errors is obtained.

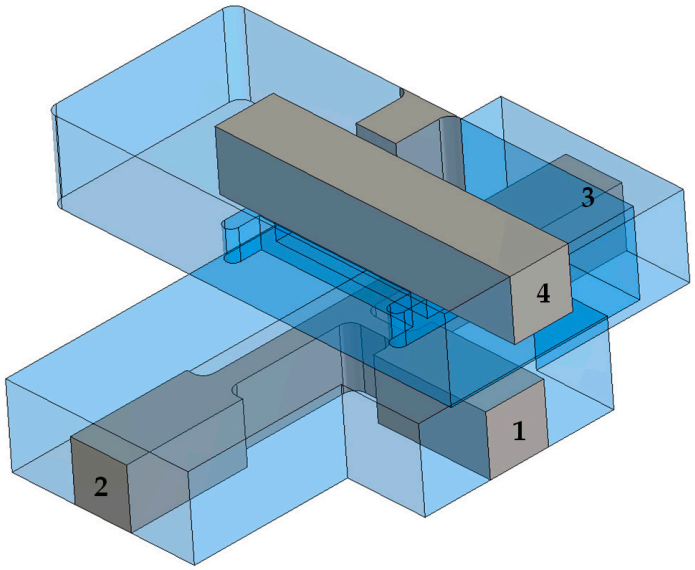

(**a**)

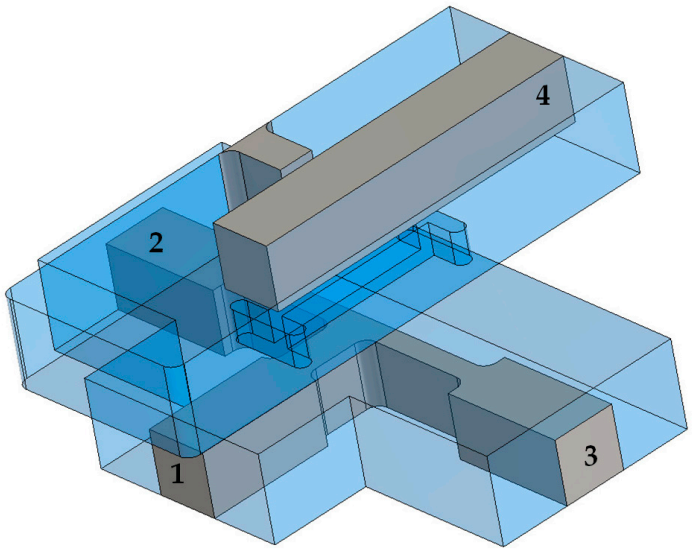

(**b**)

Figure 5. Magic-T configurations. (**a**) T-shaped (TSMT). (**b**) X-shaped (XSMT).

Table 3. Magic-T geometrical parameters.

Parameter	TSMT Value (mm)	XSMT Value (mm)	Parameter	TSMT Value (mm)	XSMT Value (mm)
a	13.00	13.00	st	2.00	2.00
b	5.50	5.50	sw	4.84	5.19
lm_1	3.24	4.24	sw_1	1.00	1.00
lm_2	9.06	8.80	sw_2	1.00	1.00
rh	4.00	4.00	wm_1	1.00	2.39
rw	4.00	4.00	wm_2	1.56	1.38
rx	6.53	6.50	xl	3.72	3.83
sh	7.47	10.82	xt	2.84	2.21
sl	12.80	12.35			

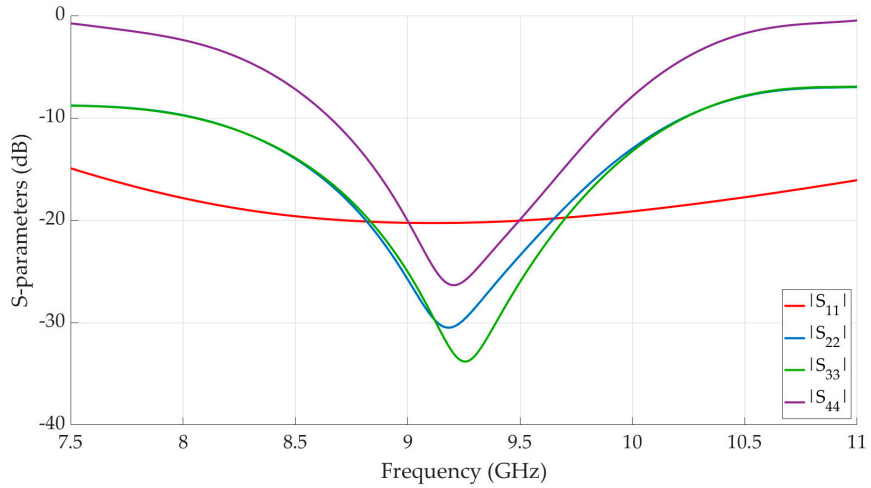

(**a**)

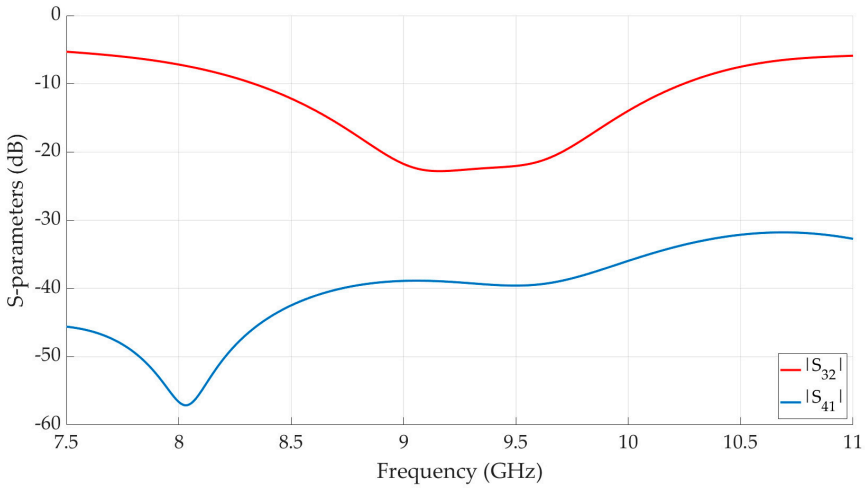

(**b**)

Figure 6. *Cont.*

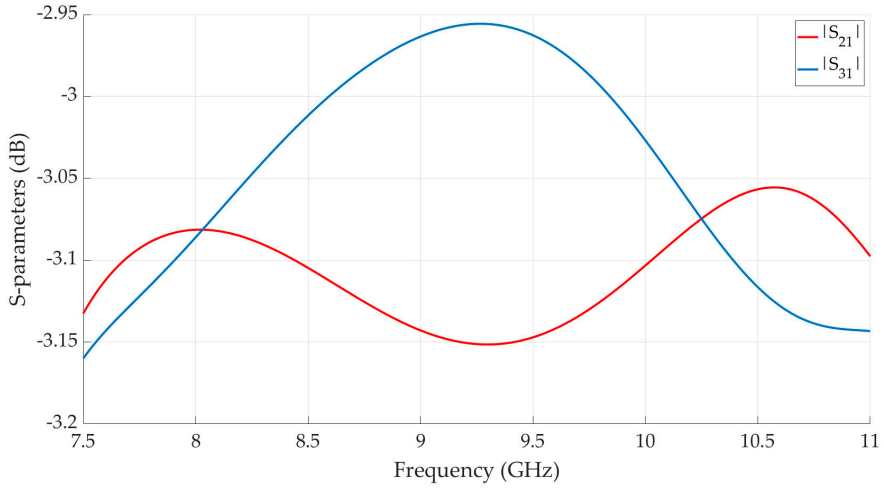

(**c**)

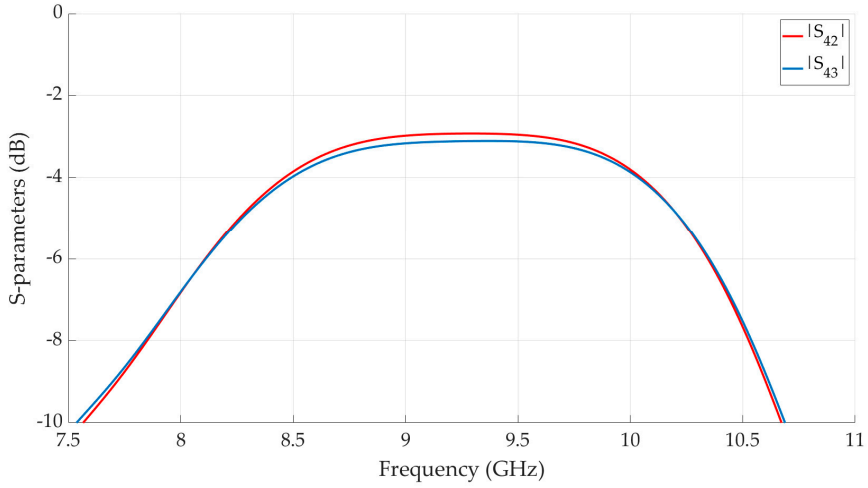

(**d**)

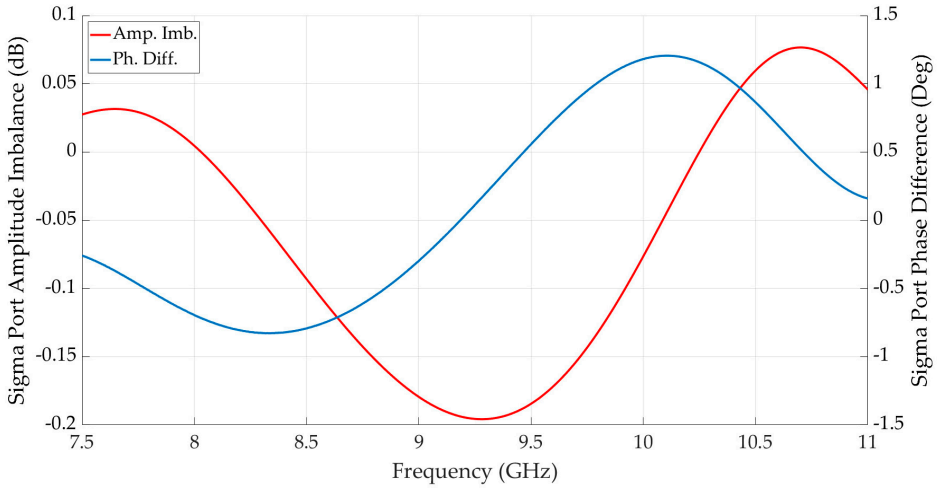

(**e**)

Figure 6. *Cont.*

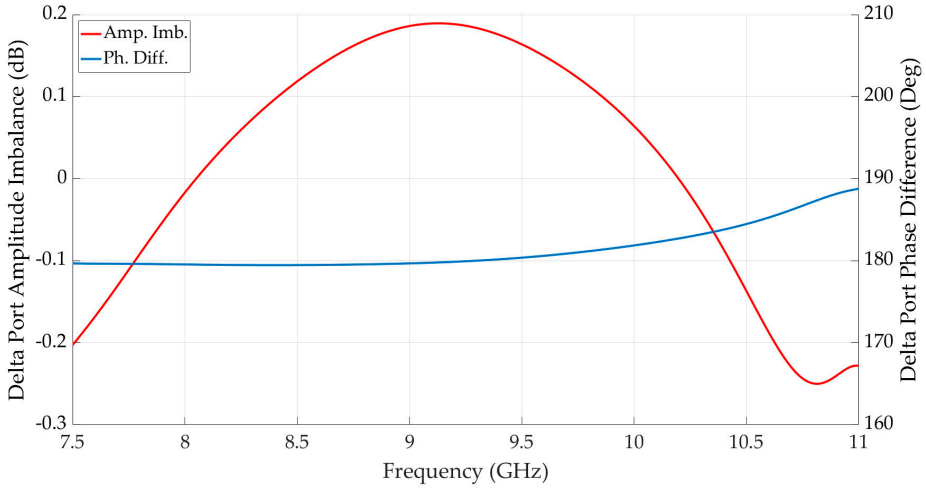

(**f**)

Figure 6. TSMT simulated S-parameters. (**a**) Input matching. (**b**) Isolation. (**c**) Transmission from sum port. (**d**) Transmission from difference port. (**e**) Sum port amplitude imbalance and phase difference. (**f**) Difference port amplitude imbalance and phase difference.

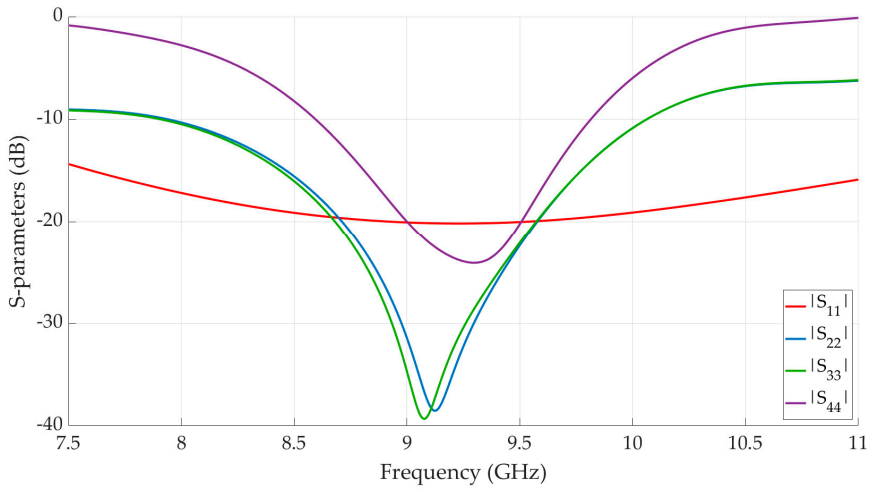

(**a**)

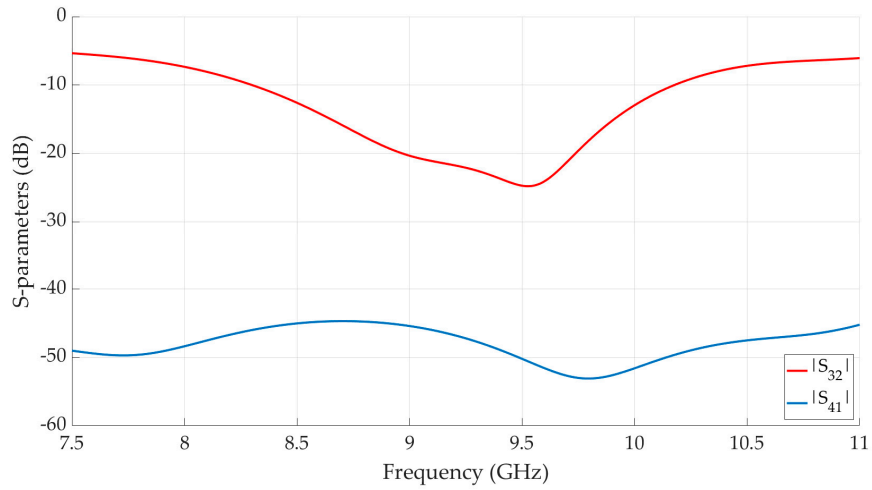

(**b**)

Figure 7. *Cont.*

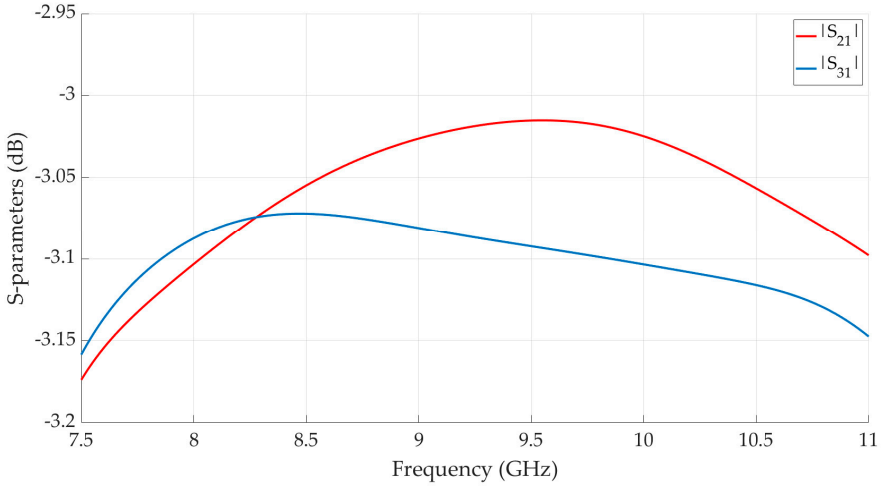

(**c**)

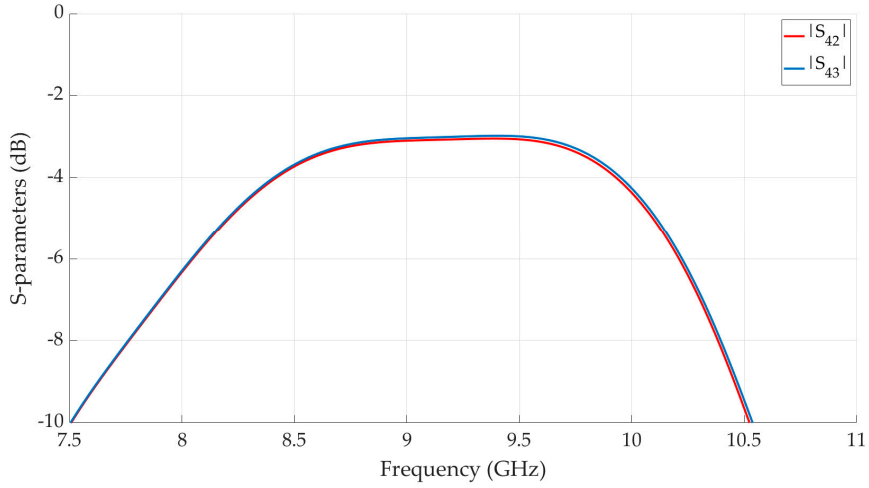

(**d**)

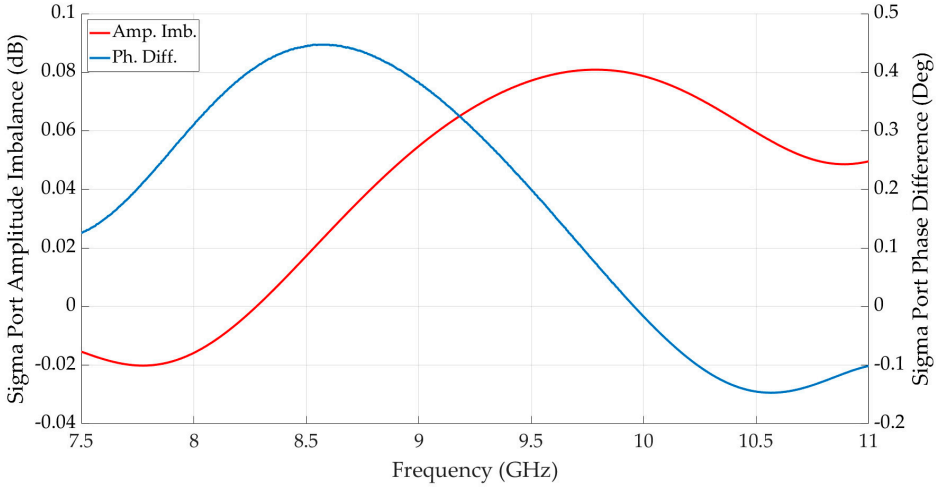

(**e**)

Figure 7. *Cont.*

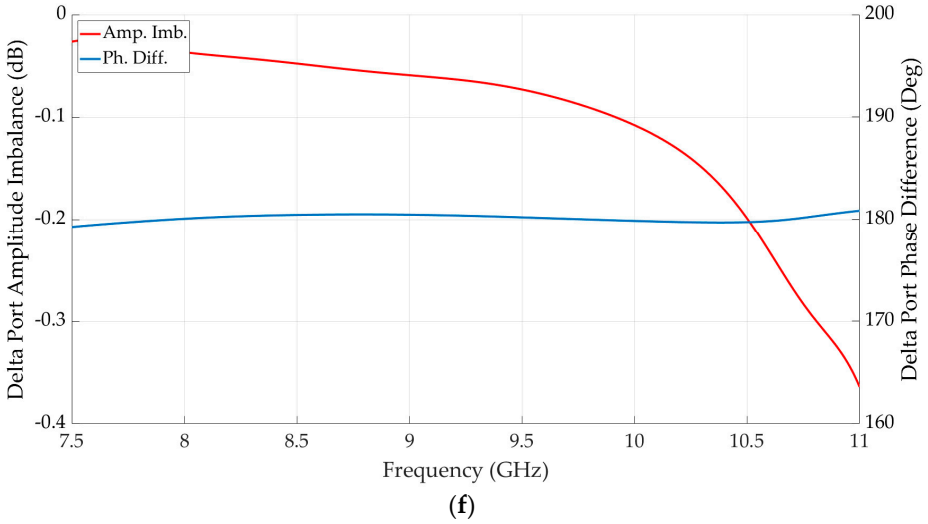

(**f**)

Figure 7. XSMT simulated S-parameters. (**a**) Input matching. (**b**) Isolation. (**c**) Transmission from sum port. (**d**) Transmission from difference port. (**e**) Sum port amplitude imbalance and phase difference. (**f**) Difference port amplitude imbalance and phase difference.

4. Magic-T Manufacturing and Test

An XSMT prototype, made of three separate parts, is realized, adopting the L-BPF additive manufacturing technique of the aluminum alloy AlSi10Mg. This material has good properties in terms of mechanical strength, weight, thermal characteristics, and workability for the post-processing phases. This alloy is widely used in sectors such as automotive and aerospace due to these peculiarities. Among various additive manufacturing techniques, L-PBF allows for the creation of lightweight, compact, and complex near-net shape components for space applications [17,18]. In this process, layers of fine metallic powders are melted layer by layer by a high-power laser. Each layer is created by fusing the layer of powder relative to the cross-sectional areas of the computer-aided design (CAD) model, which consolidates and merges with the underlying layer.

An EOSINT M270 Dual-mode system by EOS GmbH was used to build the AlSi10Mg components. This machine was equipped with a 200 W Yb-fiber laser and a beam-spot size of 100 µm. During the manufacturing process, the building chamber was filled with argon in order to keep the oxygen content less than 0.10%. The L-PBF process parameters used are shown in Table 4. The scanning direction was rotated by 67° with respect to the previous layer. The samples were built attached to the building platform and wire electrical discharge machining (EDM) cut, after stress relieving treatment at 300° for 2 h. The samples were then cleaned of non-melted powder by shot blasting with glass microspheres at a pressure of 6 bar.

Table 4. Process parameters used.

Parameter	Core	Up-Skin (2 Layers)	Down-Skin (3 Layers)	Contour
Scan speed (mm/s)	800	800	900	900
Laser power (W)	195	190	190	80
Hatching distance (mm)	0.17	0.1	0.1	

The measured surface roughness is *Ra* of 8 ± 1.3 µm and *Rz* of 62.3 ± 0.34 µm for all three parts, thus showing a certain consistency of the results obtainable with the process parameters used. Five measurements were made on each surface using the RTP80 roughness tester by SM Metrology Systems, and the arithmetic mean of such measurements was taken. The optimization of the process parameters allowed for a dimensional accuracy between

23 µm and 70 µm depending on the geometry of the component [19]. For AlSi10Mg alloy, equivalent surface electrical resistivity values of approximately 10–20 µΩ are feasible [15].

The three-layer device is shown in Figure 8. The sum and co-linear ports are included in the bottom layer, the difference port lies in the top layer, and the coupling slot is integrated in the central layer. The magic-T input ports are fed using the coaxial-to-single-ridge waveguide transition presented in [20]. Eight properly located screws guarantee good electrical contact between the three parts. Four SMA connectors complete the assembly.

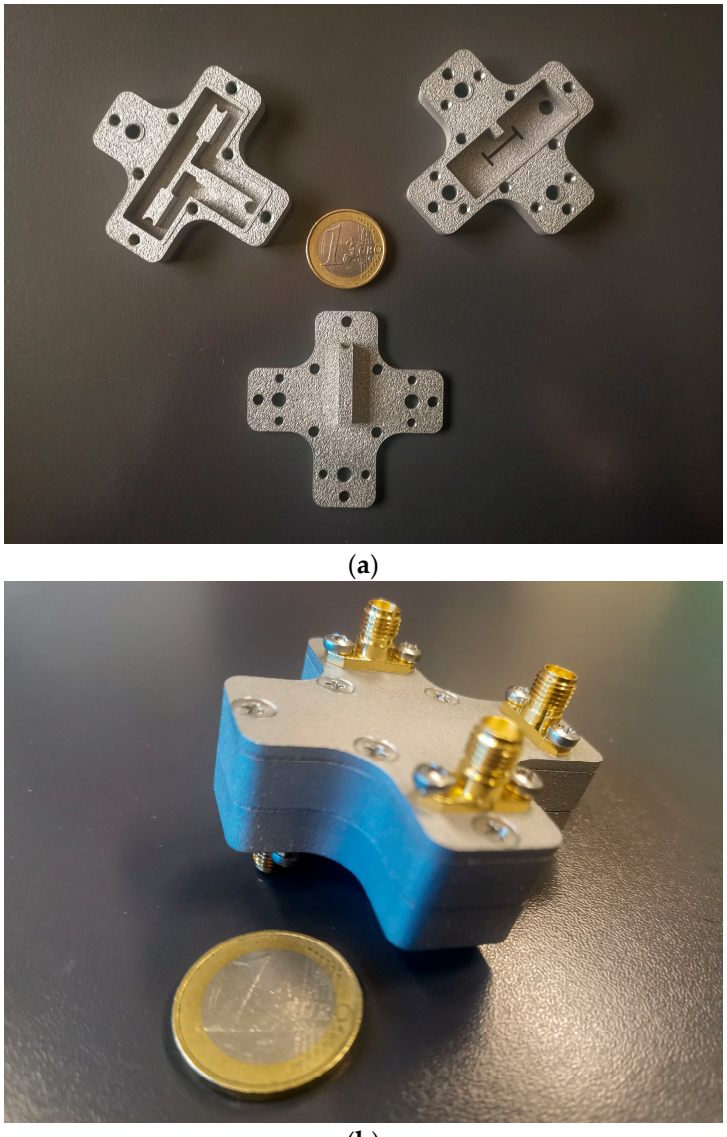

(**a**)

(**b**)

Figure 8. Manufactured XSMT prototype. (**a**) Separate parts. (**b**) Assembled device.

Measurements were performed with the N5230A vector network analyzer by Agilent. Simulation and measurement results are compared in Figure 9.

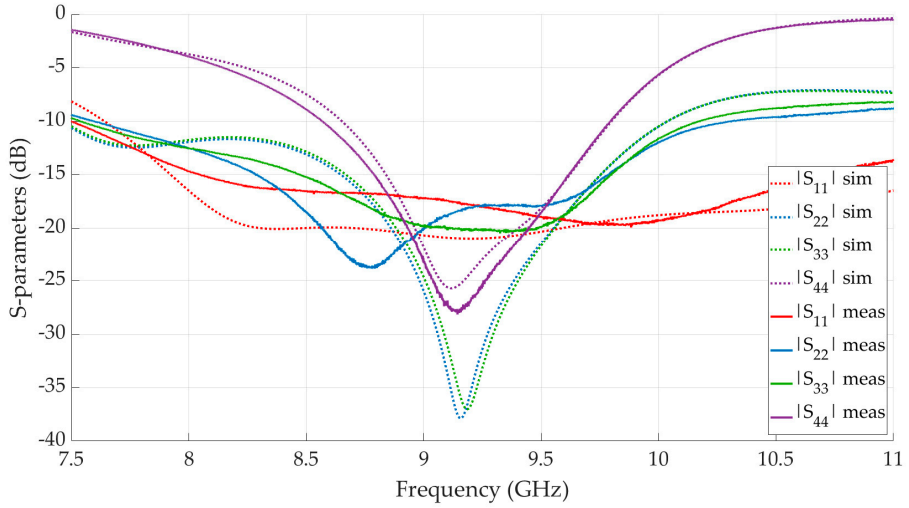

(**a**)

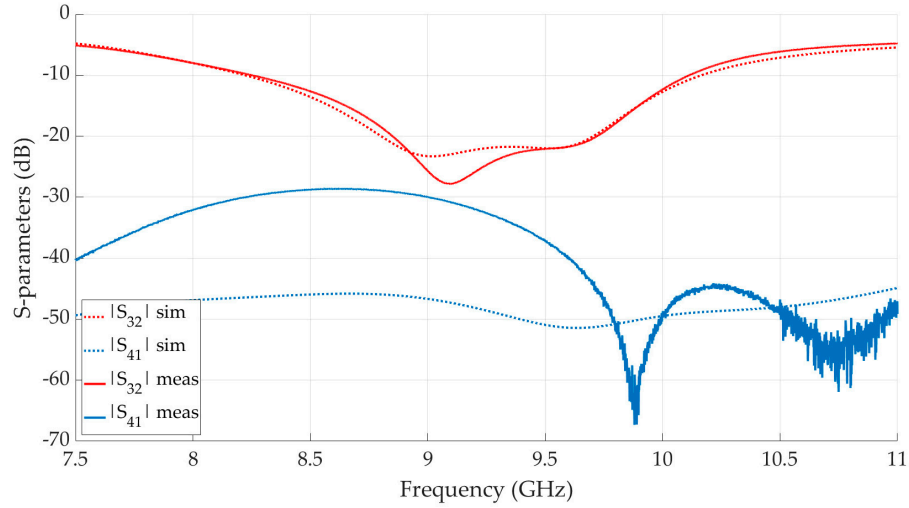

(**b**)

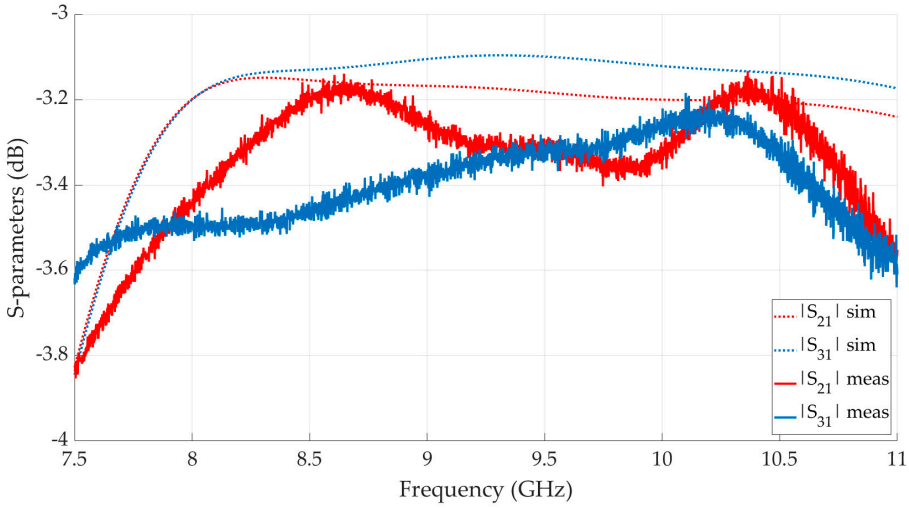

(**c**)

Figure 9. *Cont.*

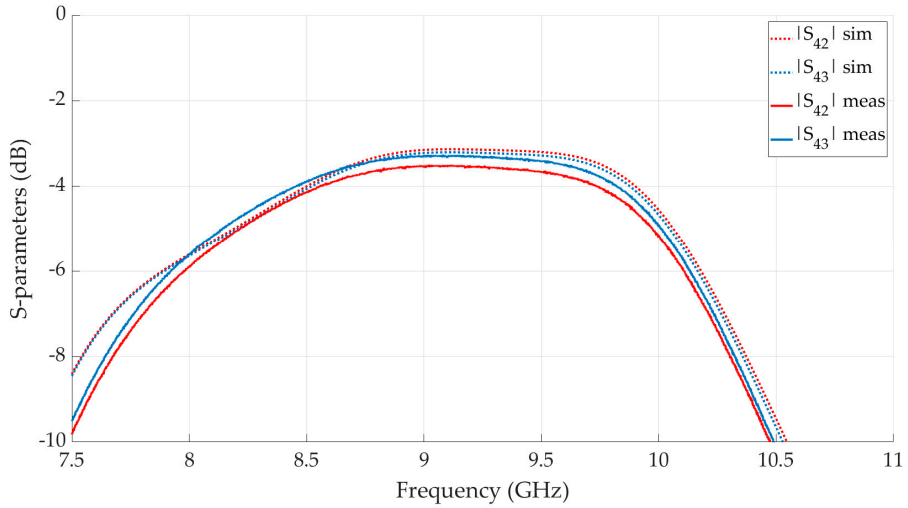

(d)

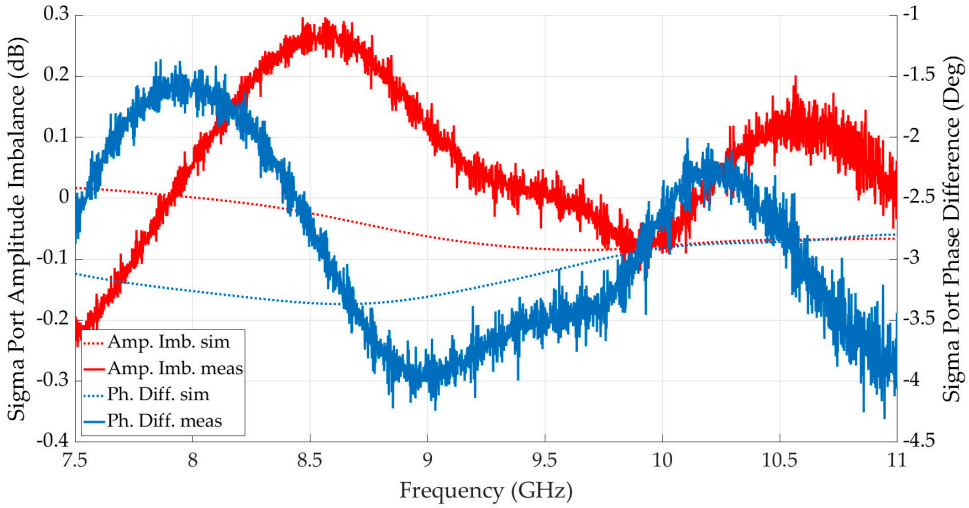

(e)

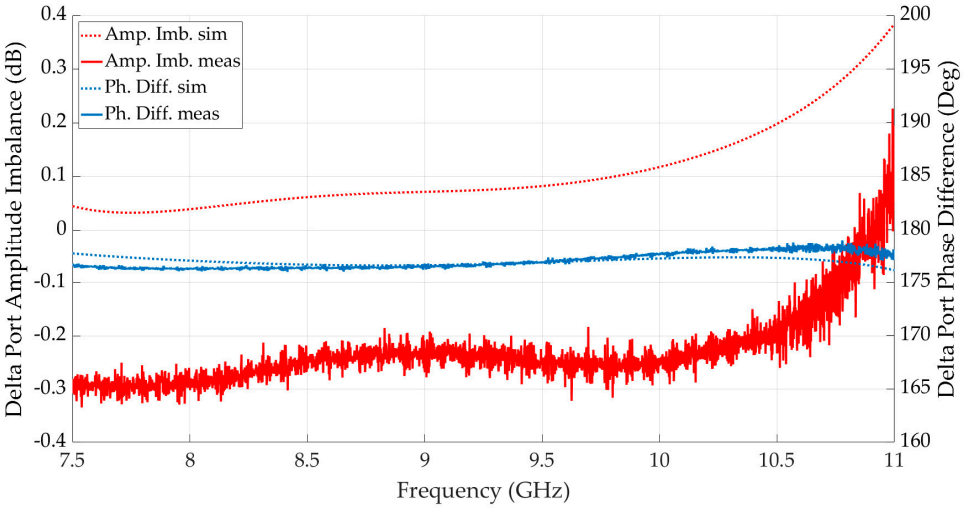

(f)

Figure 9. XSMT measured S-parameters. (**a**) Input matching. (**b**) Isolation. (**c**) Transmission from sum port. (**d**) Transmission from difference port. (**e**) Sum port amplitude imbalance and phase difference. (**f**) Difference port amplitude imbalance and phase difference.

The measured performances in the 9–9.5 GHz frequency range were in good agreement with the simulations. The discrepancy between scattering parameters levels was mainly due to the feeding transitions; in fact, it is very difficult to guarantee a nominal dimension for all four coaxial pins lengths without industrial grade accuracy. The deterioration of the isolation was caused by manufacturing tolerances and misalignment errors between layers originating during the assembly phase. Surface roughness was taken into account, assuming an equivalent conductivity of 2×10^7 for the aluminum in the simulation. Insertion losses showed an average value of 0.3 dB in the same bandwidth, which was to be imputed mainly to the coaxial connectors. This was, indeed, a very interesting result, since no significant performance degradation with respect to devices realized in standard CNC technology was observed at the X band.

5. Conclusions

An X-band low-profile single-ridge waveguide magic-T has been presented for the first time as a proper connection of two compact T-junctions in the H-plane and in the E-plane. A slot-coupling technique has been adopted such that the difference port does not extend orthogonally with respect to the sum and co-linear ports, thus making the structure quasi-planar. Two device configurations have been proposed, with sum and difference ports on the same or opposite sides of the circuit. This feature can be particularly useful in high-performance microwave applications when complex waveguide routing is required, such as in the design of monopulse comparator networks for radar systems. Matching elements have been integrated in the waveguide layers, thus noticeably simplifying the manufacturing process. An AlSi10Mg aluminum alloy prototype has been fabricated using L-PBF additive manufacturing technique and a good agreement between simulated and measured results has been observed. In particular, the insertion loss performance is noteworthy, basically assessing an equivalence between the adopted manufacturing technique and standard CNC milling machine processes.

Author Contributions: Conceptualization, R.R. and R.V.G.; methodology, R.R. and R.V.G.; software, R.V.G.; validation, R.R. and R.V.G.; formal analysis, R.R. and R.V.G.; investigation, R.R.; resources, R.V.G., F.C., L.I. and S.C.; data curation, R.R.; writing—original draft preparation, R.R.; writing—review and editing, R.R., R.V.G., F.C., L.I. and S.C.; visualization, R.R. and R.V.G.; supervision, R.V.G.; project administration, R.V.G., F.C. and L.I.; funding acquisition, S.C. All authors have read and agreed to the published version of the manuscript.

Funding: This research was funded by Elettronica Aster S.p.A. and the Italian MiSE (Ministry of Economic Development), ex legge 808/85, codice di domanda 2017-N-0858-C.

Institutional Review Board Statement: Not applicable.

Informed Consent Statement: Not applicable.

Data Availability Statement: Generated data is contained within the article.

Acknowledgments: The authors would like to thank Elettronica Aster S.p.A. management team for funding this project.

Conflicts of Interest: The authors declare no conflict of interest.

References

1. Pozar, D. *Microwave Engineering*, 4th ed.; John Wiley & Sons: Hoboken, NJ, USA, 2011.
2. Gatti, R.V.; Rossi, R. A dual-polarization slotted waveguide array antenna with polarization-tracking capability and reduced sidelobe level. *IEEE Trans. Antennas Propag.* **2016**, *64*, 1567–1572. [CrossRef]
3. Gatti, R.V.; Rossi, R. A dual circularly polarized slot-fed horn array antenna with linear polarization tracking feature. *Wiley Int. J. RF Microw. Comput.-Aided Eng.* **2018**, *28*, e21480. [CrossRef]
4. Hopfer, S. The design of ridged waveguides. *IRE Trans. Microw. Theory Technol.* **1955**, *3*, 20–29. [CrossRef]
5. He, Y.-J.; Mo, D.-Y.; Wu, Q.-S.; Chu, Q.-X. A ka-band waveguide magic-t with coplanar arms using ridge-waveguide transition. *IEEE Microw. Wirel. Compon. Lett.* **2017**, *27*, 965–967. [CrossRef]

6. Guo, L.; Li, J.; Huang, W.; Shao, H.; Ba, T.; Jiang, T.; Jiang, Y.; Deng, G. A waveguide magic-t with coplanar arms for high-power solid-state power combining. *IEEE Trans. Microw. Theory Technol.* **2017**, *65*, 2942–2952. [CrossRef]
7. Bunn, H.; Whitten, C. Ridged Waveguide Magic Tee. Patent US3315183A, University of California. 1967. Available online: https://patents.google.com/patent/US3315183 (accessed on 12 September 2022).
8. Siekanowicz, W.; Paglione, R. Broadband Double-Ridge Waveguide Magic Tee, Patent US3629734A, RCA Corp. 1971. Available online: https://patents.google.com/patent/US3629734A/en (accessed on 12 September 2022).
9. Yuan, C.; Luo, Y.; Meng, F.; Chen, G. A full-frequency band matching structure of double-ridge magic t. In *Proceedings of the 2016 2nd International Conference on Advances in Energy, Environment and Chemical Engineering (AEECE 2016)*; Springer Nature: Berlin/Heidelberg, Germany, 2016. [CrossRef]
10. Wu, J.; Wang, C.; Guo, Y. Ridged waveguide magic tees based on 3-d printing technology. *IEEE Trans. Microw. Theory Technol.* **2020**, *68*, 4267–4275. [CrossRef]
11. Gatti, R.V.; Rossi, R.; Dionigi, M.; Spigarelli, A. An x-band compact and low-profile waveguide magic-t. *Wiley Int. J. RF Microw. Comput.-Aided Eng.* **2019**, *29*, e21854. [CrossRef]
12. Rossi, R.; Gatti, R.V. An h-plane groove gap waveguide magic-t for x-band applications. *Electronics* **2022**, *11*, 4075. [CrossRef]
13. Huang, G.-L.; Zhou, S.-G.; Chio, T.-H.; Yeo, T.-S. Two types of waveguide comparator for wideband monopulse antenna array application. In Proceedings of the 2015 IEEE 5th Asia-Pacific Conference on Synthetic Aperture Radar (APSAR), Singapore, 1–4 September 2015. [CrossRef]
14. Singh, Y.; Chakrabarty, A. Design and sensitivity analysis of highly compact comparator for ku-band monopulse radar. In Proceedings of the 2006 International Radar Symposium, Krakow, Poland, 24–26 May 2006. [CrossRef]
15. Mohammadi, M.; Kashani, F.; Ghalibafan, J. A compact planar monopulse combining network at w-band. In Proceedings of the 2009 5th IEEE GCC Conference & Exhibition, Kuwait, 17–19 March 2009. [CrossRef]
16. Mohammadi, M.; Kashani, F. Planar eight port waveguide mono-pulse comparator. *Prog. Electromagn. Res. C* **2009**, *6*, 103–113. [CrossRef]
17. Peverini, O.; Addamo, G.; Lumia, M.; Virone, G.; Calignano, F.; Lorusso, M.; Manfredi, D. Additive manufacturing of ku/k-band waveguide filters: A comparative analysis among selective-laser melting and stereo-lithography, IET Microwave. *Antennas Propag.* **2017**, *11*, 1936–1942. [CrossRef]
18. Van Caekenberghe, K.; Bleys, P.; Craeghs, T.; Pelk, M.; Van Bael, S. A w-band waveguide fabricated using selective laser melting. *Wiley Microw. Opt. Technol. Lett.* **2012**, *54*, 2572–2575. [CrossRef]
19. Calignano, F.; Peverini, O.; Addamo, G.; Iuliano, L. Accuracy of complex internal channels produced by laser powder bed fusion process. *J. Manuf. Process.* **2020**, *54*, 48–53. [CrossRef]
20. Gatti, R.V.; Rossi, R.; Dionigi, M. X-band right-angle coaxial-to-single ridge waveguide compact transition with capacitive coupling. *IET Electron. Lett.* **2019**, *55*, 103–105. [CrossRef]